express
polymer letters

Research article

Observation of heterogeneities in elastocaloric natural/wastes rubber composites

Nicolas Candau[1][*], *Eduard Vives*[2], *Ana Inés Fernández*[3], *Oguzhan Oguz*[4,5],
Guillaume Corvec[6], *Carlos Eloy Federico*[7], *João Paulo Cosas Fernandes*[7],
Gregory Stoclet[8], *Maria Lluïsa Maspoch*[1]

[1]Centre Català del Plàstic (CCP) – Universitat Politècnica de Catalunya Barcelona Tech (EEBE-UPC), Av. D'Eduard Maristany, 16, 08019 Barcelona, Spain
[2]Departament de Física de la Matèria Condensada, Facultat de Física, Universitat de Barcelona, Martí i Franquès 1–11, 08028 Barcelona, Spain
[3]Department of Materials Science and Physical Chemistry, Universitat de Barcelona, Martí i Franquès 1–11, 08028 Barcelona, Spain
[4]Faculty of Engineering and Natural Sciences, Materials Science and Nano Engineering, Sabanci University, 34956 Orhanli, Turkey
[5]Sabanci University Integrated Manufacturing Technologies Research and Application Center & Composite Technologies Center of Excellence, Teknopark Istanbul, Turkey
[6]Mines ParisTech, PSL Research University, CEMEF – Centre de Mise en Forme des Matériaux, UMR CNRS 7635, CS 10207, Sophia-Antipolis 06904, France
[7]Department of Materials Research and Technology (MRT), Luxembourg Institute of Science and Technology (LIST), L-4362 Esch-sur-Alzette, Luxembourg
[8]Université de Lille, CNRS, INRAE, Centrale Lille, UMR 8207 - UMET – Unité Matériaux et Transformations, F-59000 Lille, France

Abstract. The strain-induced crystallization and elastocaloric properties of various natural rubber (NR)/ground tire rubber (GTR) blends, comprising waste particles of diverse sizes and contents, were investigated. The decreasing inter-distance between particles in conjunction with their increasing content as studied by micro-computed tomography (μCT) as well as the inter-melling between GTR and NR matrix were observed. It resulted in a strain localization in the NR matrix at the GTR and NR interface at the origin of mechanical reinforcement upon tensile deformation. In addition, GTR particles were found to show a nucleating ability on strain-induced crystallization (SIC) and elastocaloric properties independently of the particle size. The strain localization was found to relate to a localization of the temperature field, suggesting localization of the elastocaloric effect in NR/GTR blends. The evidence of such heterogeneities would be of interest for the proper design of elastocaloric waste-based rubber composites for heating/cooling applications.

Keywords: *rubber, recycling, material testing, elastocaloric properties, materials for energy*

1. Introduction

The regulation of the increase of the temperature on the surface of our planet requires the development of sustainable energy technologies that limit the emission of green-houses gases [1]. Conventional vapor-compression technology has dominated heating/cooling/refrigeration (H/C/R) applications but uses toxic gases (carbon dioxide, ammonia) and

---

refrigerants (hydrofluorocarbons) that contribute to the greenhouse effect [2]. Solid-state caloric systems based on magnetocaloric (MC), electrocaloric (EC), barocaloric (BC), and elastocaloric (eC) technology are promising candidates for replacing vapor/compression systems in urban environments [3]. Within the last decades, several publications on the MC effect [4], the EC effect [5], the eC effect [6] and the BC effect [7] renewed interest in heating/cooling technology.

Nonetheless, caloric materials do not fully assess the environmental question, are expensive and prone to supply shortages as they require rare-earth elements (*e.g.*, Gadolinium (Gd), Neodymium (Nd), or Praseodymium (Pr)) [8]. Hence, new eco-friendly caloric materials still need to be developed. Among the above-mentioned existing caloric systems, eC cooling technology is an encouraging green alternative [9]. The specificity of eC materials is their ability to generate heating/cooling upon deformation due to entropic elasticity and strain-induced phase transition. However, the main limitation for these materials, like shape memory alloys (SMA's) [10], is the huge amount of mechanical energy necessary to initiate phase transition (hundreds of megapascals), thus limiting their efficient usage in commercial applications. To overcome SMA's efficiency limitation in heating/cooling applications, giant elastocaloric rubbery materials such as polyurethane (TPU) [11] or natural rubber (NR) [12] can be used owing to their crystallization ability [13, 14], usually found higher as compared to other synthetic rubbers [15, 16]. Reinforcing fillers commonly incorporated into NR, such as carbon black fillers [17, 18], silica [19], graphene oxides [20] or clay [21], are known to act as nucleating agents for promoting strain-induced crystallization (SIC) in NR-based composites. Mechanical properties of NR-based materials containing waste rubber, such as waste chloroprene rubber (CR) [22], waste latex [23] or tire wastes [24] have also been extensive. The nucleation ability of the wastes (type GTR) on SIC of NR had been identified by direct *in-situ* X-rays measures [25] and indirect infrared thermography [26]. All these NR-based materials hence show promising elastocaloric properties.

Among the class of caloric materials, natural rubber exhibits unique properties such as bio-based nature, softness, cheapness, biodegradability and recyclability, simultaneously suitable for solving engineering and sustainability issues in heat pump applications.

It was suggested that the temperature rises at NR surface upon rapid loading was ascribed to the strain-induced crystallization as shown by X-rays [27]. The occurrence of SIC in NR was modeled by Flory [28], which served as a basis for the development of more recent approaches such as micro-mechanical [29, 30] or phase field modeling [31].

The elastocaloric effect (eC) in natural rubber, mostly originating from SIC, is widely investigated [32, 33, 12, 34], by optimizing and understanding the effect of pre-stretching and cycling, [32] of the strain rate and temperature [34]. The strain-induced crystallization kinetics of natural rubber can be modified by imposing diverse pre-strain, having a direct consequence on the kinetics of the eC effect. For instance, from a pre-stretch of 300 to 600%, the characteristic crystallization time was found to decrease from several hundred milliseconds to a few decades of milliseconds [35]. In terms of elastocaloric applications, the temperature at the NR surface can hence be modified quickly up to a decade of degrees. In addition, NR, as soft material, requires weak mechanical energy to induce eC effect, which is found two orders of magnitude lower than in caloric shape memory alloys, making this material a promising candidate for suitable heat pump applications.

In spite of its bio-based nature and degradability, natural rubber is a highly demanded material extracted from the Hevea tree that still does not fully comply with ecological demand. While other sources of NR had been recently proposed, such as Dandelion or Guayule, its partial replacement by waste rubber can be chosen as an alternative ecological option [36, 37], while the preparation of composites incorporating wastes can show some limitations in terms of mechanical performance. Nonetheless, the use of waste rubber with SIC abilities, [22, 23], in an NR matrix improves the mechanical reinforcement of the resulting composite. While not directly shown by the in situ wide angle X-rays scattering (WAXS) technique, such reinforcement was assumed to be due to their enhanced SIC ability.

In spite of such promising SIC ability and possible resulting eC effect in the above-mentioned natural/waste rubber blends, these rubber composites incorporating wastes were rarely used as candidates for heating/cooling technologies. Among the rare published works, the barocaloric effects in natural/waste rubber blends have been characterized [38]. In previous works, we also prepared peroxide vulcanized

natural rubber (NR)/ground tire rubber (GTR) composites by combining mechanical testing and in situ WAXS [25]. It was found that the incorporation of GTR into the NR matrix led to reinforcement at large strains at room temperature attributed to (i) the presence of the GTR particles acting as reinforcing fillers and (ii) the nucleating effect of the GTR for SIC in the NR matrix. The elastocaloric effect in the same materials was then characterized by combining in situ infrared thermography and a thermodynamic frame [26]. Beneficial eC effect has been shown for the vulcanized natural/waste rubber blend up to 20 wt% of wastes, as compared to the pristine vulcanized NR. It was ascribed to increased strain localization and an improved latent heat due to the nucleation effect of the GTR particles on SIC in NR. However, no observation of the heterogeneities of the waste particles in relation to the elastocaloric response of the resulting composite had been conducted. One may note that such work has been extensively done in metallic materials. As non-exhaustive examples, heterogeneities in the strain field and their response have been studied to identify plastic mechanisms in metallic materials such as Portevin–Le Chatelier plastic instabilities [39], the local grain deformation in polycrystalline metals [40], or anisotropic temperature field in oriented materials [41]. Heterogeneities in temperature rise had also been observed in polymeric systems, namely granular TPUs in the contact zone of the grains due to high-stress concentration [42].

In this paper, we aim to investigate the heterogeneities of a wide variety of vulcanized NR/GTR blends containing wastes GTR particles with diverse average sizes and content. The heterogeneities of the waste particles structure, as well as heterogeneities in the resulting NR/GTR composites, were exanimated and their influence on crystallization ability and elastocaloric effects were discussed. In particular, the presence of waste rubber particles was found to modify the temperature field during both heating and cooling, from a ligament type feature to a sea island type feature showing temperature fluctuations that we state to be ascribed to strain localization in the regions near the reinforcing waste particles.

2. Materials and experiments
2.1. Materials and processing
The NR of this study is an SMR (Standard Malaysian Rubber) CV60 (Mooney viscosity ML 1+4, 100 °C: 55-60), supplied by the company Akrochem (USA),

with 0.15% of hydroxylamine added to the latex stage to prevent the raw rubber stiffening while storing. GTR was supplied by the company J. Allcock & Sons Ltd (United Kingdom) using the transformation of used tire buffing into finer rubber crumbs via a controlled cryo-grinding. GTR is composed of rubber (85 wt% of natural rubber, and 15 wt% of styrene butadiene rubber) and carbon black (CB). It also contains additives from sulphur vulcanization (see scanning electron microscopy and energy dispersive X-rays spectroscopy – SEM-EDX images in [43]). The GTR crumbs are free of contaminants such as textile, metal and road dirt. The GTR particles were subsequently sieved using a vibratory sieve shaker (Analysette 3, Germany) with a different mesh size of 80 (size <180 μm), and 120 (size <125 μm), and 230 (size <63 μm). The quantity of CB may vary depending on the collected sizes. Thermogravimetry analysis (TGA) and derivative thermogravimetry (DTG) curves of the GTR were provided in [43] and suggested that the non-rubber components (mostly CB fraction) may reach a mass fraction of 45 wt%. Before processing, the GTR particles were dried overnight in a vacuum oven (Vaciotem-TV, J.P. SELECTA®, Spain) over silica gel at 70 °C to prevent humidity absorption. The natural rubber was masticated inside the chamber of an internal mixer (Brabender Plasti-Corder W50EHT, Brabender GmbH & Co., Germany, volume chamber 55 cm^3) at a temperature of 80 °C, for 5 minutes and a rotation speed of 40 rpm. After 5 minutes of mastication, the GTR was added. After 5 more minutes the vulcanizing agent dicumyl peroxide (DCP) was added (1.5 wt% of the NR) and mixed for 5 minutes. The masterbatch containing NR, GTR, and DCP was vulcanized according to the estimated optimal time at 170 °C [44] under 4 MPa. In order to perform the tensile tests, dogbone-shaped specimens with a 1 mm thickness, 4 mm width, and 15 mm length were extracted from hot molded sheets by die-cutting with a specimen preparation punching machine (CEAST). Table 1 gives the composition and properties of the prepared materials.

2.2. Micro-computed X-ray tomography (μCT)
3D morphological information of GTR was obtained by micro-computed X-ray tomography (μCT) carried out by a RX Solutions EasyTom 160 scanner using a tungsten filament. An acceleration voltage of 40 kV and a current of 80 μA were employed with a frame

Table 1. Specimen nomenclature, composition and thermal properties at room temperature.

Sample code	Natural rubber [wt%]	Ground tire rubber [wt%]	Mesh size of the sieve [1/inch]
NR	100	0	–
NR/GTR10 120's	90	10	120
NR/GTR20 120's	80	20	120
NR/GTR33 80's	67	33	80
NR/GTR33 120's	67	33	120
NR/GTR33 230's	67	33	230

rate of 1.5 while averaging five frames per projection. A full rotation (360°) was used with projections taken every 0.25°. The source-to-object-distance (SOD) and source-to-detector-distance (SDD) were set to obtain a voxel size of 2 μm. The 3D volume reconstruction of the projections was generated by the software Xact64. Image treatment and analysis were performed with the commercial software Avizo (Thermo Fisher Scientific). The inherent noise of the acquired images was reduced by means of a median filter. Then, GTR particles in the images were binarized by thresholding the grayscale histogram. A watershed algorithm was used for separating close objects. Next, elements represented by less than 3 voxels were removed to decrease uncertainties due to their limited geometrical representation. This procedure enabled a spatial resolution of 7 μm, corresponding to the smallest object detected with accuracy. Finally, the binarized objects were characterized firstly by their inter-particle distance, which is determined by the computation of the Euclidean distance map of particles, and secondly by the particles' equivalent diameter (D_{eq}) defined as Equation (1) [45]:

$$D_{eq} = \sqrt[3]{\frac{6V}{\pi}} \tag{1}$$

where V corresponds to the volume of the particles.

2.3. Atomic force microscopy (AFM)

Images of the topography and nanomechanical properties of the samples were acquired using the AM-FM mode of the MFP-3D Infinity AFM (Asylum Research). All measurements were made under ambient conditions (room temperature and relative humidity of about 50%) and a standard cantilever holder for operation in the air was used. Images with an area of 20×20 μm² or 5×5 μm² were taken with a resolution of 512×512 pixels at a scan rate of 2 Hz. Cantilevers' spring constants used in this study were

about 30 N/m (AC160TS-R3 model from Olympus). The first and second resonant frequencies for AC160TS-R3 cantilever were about 280 kHz and ~1.6 MHz, respectively. A relative calibration method was done to estimate the tip radius using a dedicated reference samples kit supplied by Bruker (Model: PFQNM-SMPKIT-12m). The deflection sensitivity and the spring constant of the cantilever were determined using the GetReal™ Automated Probe Calibration feature. The tip radius was adjusted to obtain the proper value of 2.7 GPa for the polystyrene reference. To ensure repulsive intermittent contact mode, the amplitude setpoint was chosen as Asetpoint/A0 ~ 0.20 so that the phase was well fixed below 90°.

2.4. *In-situ* wide angle X-rays (WAXS)

A miniature tensile test machine was used to record 2D-WAXS patterns from specimens subjected to tensile strains at 10 mm·min⁻¹. Tensile test bars with a 0.5×4 mm² rectangular cross-section and 5 mm gauge length were prepared. The experiments were carried out owing to a Xeuss 2.0 apparatus (Xenocs) and the two-dimensional X-rays scattering patterns were recorded by a Pilatus 200k hybrid pixel detector (Dectris) with a specimen-detector distance of 140 mm. The experiments were performed in transmission mode with a beam size of 500 μm×500 μm. During the tensile deformation, X-rays patterns are recorded, each of them results from an exposure of 30 seconds to the X-rays beam, corresponding to the recording of a scattering pattern every 5 mm of displacement of the specimen. The measured diffracted X-rays intensity collected on the 2D detector must be corrected from the presence of air scattering, direct beam scattering and scattering variations due to changes in the specimen thickness. The intensity I_d due to air scattering and direct beam were measured in the absence of any sample. It was removed from the measured intensity scattered in the presence of the material Imeas. The corrected scattering intensity Icorr is written: $I_{corr} = I_{meas} - TI_d$ with T, the transmission factor is equal to $e^{-\mu e}$, μ is the coefficient of transmission and e the thickness of the specimen. Assuming conservation of the specimen volume during tensile deformation, a longitudinal deformation of $1 + \lambda$, with λ the stretching ratio results in a reduction of its width and thickness of $1/\lambda^{1/2}$. Hence the thickness of the specimen, e, is equal to $e_0/\lambda^{1/2}$. Each scattering pattern was integrated azimuthally (radial direction θ of the scattering pattern). The deconvolution

of the curve $I = f(2\theta)$ enabled the extraction of the intensity at the peak top and the width at half height of each crystalline peak, and the intensity at the peak top of the amorphous phase. The crystallinity index *CI* was then determined as Equation (2):

$$CI = \frac{I_c}{I_a + I_c} \qquad (2)$$

where I_c and I_a are the intensity of the crystalline and amorphous peaks respectively.

2.5. Tensile tests with *in-situ* infra-red thermography measurements

Incremental uniaxial tensile tests have been performed up to various strains up to failure, at the speeds of 14 mm·s⁻¹. The specimens have a gauge length of 15 mm, so the nominal strain rate was estimated equal to $5.6 \cdot 10^1$ min⁻¹. The tension testing machine is an electromechanical Zwick 2.5 kN equipped with a load sensor of 100 N. During the tests, the sample temperature was recorded by means of an infrared camera which is a Cedip Silver (Flir). The infrared sensor is 320×240 pixels, and the spatial resolution is 620 μm per pixel. The camera was turned on at least 3 hours before the tests such that its internal temperature stabilizes. The acquisition frequency is 25 Hz. The (non-uniformity correction of the captor (CNUC) was used with a homemade calibration. The corresponding polynomial, unique for all pixels, is $T(DL) = -7.8827 \cdot 10^1 + 2.3105 \cdot 10^{-2} \cdot DL - 1.5942 \cdot 10^{-6} \cdot DL^2 + 4.2811 \cdot 10^{-11} DL^3$, where *DL* stands for digital level. Because of the large deformations imposed on the samples, a motion compensation technique was used in order to obtain the temperature at the sample center during the duration of the tests. This was achieved by computing a marker tracking algorithm on the infrared images. A specific target with a high emissivity contrast was fixed to the moving clamp. At the initial state of the tests, the coordinates of the edges of the clamps were manually set using the contrast between the clamps and the background. The distance between the target and the edge of the moving clamp was assumed constant. The horizontal coordinate of the center of the sample was also assumed to be constant. At each time (or image) the vertical coordinate of the center of the sample was computed to correspond to the mid-distance between the clamps.

2.6. High-resolution infra-red thermography measurements

Room temperature uniaxial tensile tests were performed on a universal testing machine Zwick/Roell (Z005) equipped with a 5 kN force sensor. The crosshead speed during the loading and unloading phases was chosen to equal 3000 mm·min⁻¹, corresponding to a nominal strain rate of $2 \cdot 10^2$ min⁻¹ according to the specimen dimensions (15 mm length). The rubber specimens were stretched up to a deformation of 500% followed by a relaxation step in the deformed state for one minute. After the relaxation step, the specimens were unloaded with the same nominal strain rate of $2 \cdot 10^2$ min⁻¹ down to the relaxed state (zero force), followed by another relaxation for one more minute. The temperature field on the front face of the samples was recorded using an Infra-red camera (InfraTech ImageIR® 8800) equipped with a mercury-cadmium-telluride (MCT) detector with a temperature resolution at 30 °C higher than 0.035 K. The distance between the IR camera and the specimen was chosen to be sufficiently close (60 mm) to ensure a spatial resolution sufficiently high, allowing to record images with fine pixel size (15 μm). The size of the observation zone is 64×64 pixels² (1×1 mm²). Image data was synchronized with analogical data of the tensile test machine, namely time, force and displacement between the grips. The acquisition frequency of the IR images was chosen equal to 100 Hz in order to capture fast temperature changes that may occur within the different phases of the tests. These frequencies are high enough to ensure a sufficiently low strain increment between two images during the loading and/or unloading (maximum of 8% of deformation) or sufficiently fast acquisition time during relaxation steps (10 ms). The IRBIS 3.1 professional software (InfraTech ImageIR® 8800) was used to extract punctual temperature values along the specimen longitudinal axis. The central part of the specimen where the temperature data was extracted shows a rather homogeneous temperature field at the mm scale.

3. Results and discussion
3.1. Morphological and nanomechanical properties

Ground tire rubber particles (GTR) sieved with different mesh sizes (Table 1) were mixed with natural rubber (NR) from 0 to 33 wt% and vulcanized under

hot press. 3D representative tomography images of the obtained vulcanized NR/GTR composites (Figure 1a) were performed for each type of blend to quantify the size distribution of the GTR particles (Figure 1b) as well as the distribution of their inter-distance (Figure 1c). The average inter-distance between particles widely decreases while increasing the quantity of waste particles (Figure 1d) due to a spread toward smaller values while increasing the GTR content. The slight decrease in the measured average particle diameter while increasing the waste quantities in the blends is consistent with the absence of particle agglomeration that could have resulted from blending and/or curing. While increasing the sieving size, the equivalent diameter distribution is found to broaden to larger values (Figure 1c). As a result, the median

equivalent diameter significantly increases. Contrarily, the median average inter-distance between particles is found to be almost invariant with the sieving size (Figure 1e). The effect of GTR particle size distribution and inter-distances on tensile properties will be presented in the following.

To get deeper insight on internal and interfacial heterogeneities in the waste rubber particles properties, AFM experiments were performed on the NR/GTR blends. Interfaces between matrix and GTR particles are clearly seen in phase (Figure 2a) and modulus cartographies (Figure 2b). GTR particles on the bottom present a low phase (dark gray) and higher modulus (yellow) than the NR matrix. In some images, the interface seems to be continuous, with a probable intermelling of the NR matrix with the GTR particle,
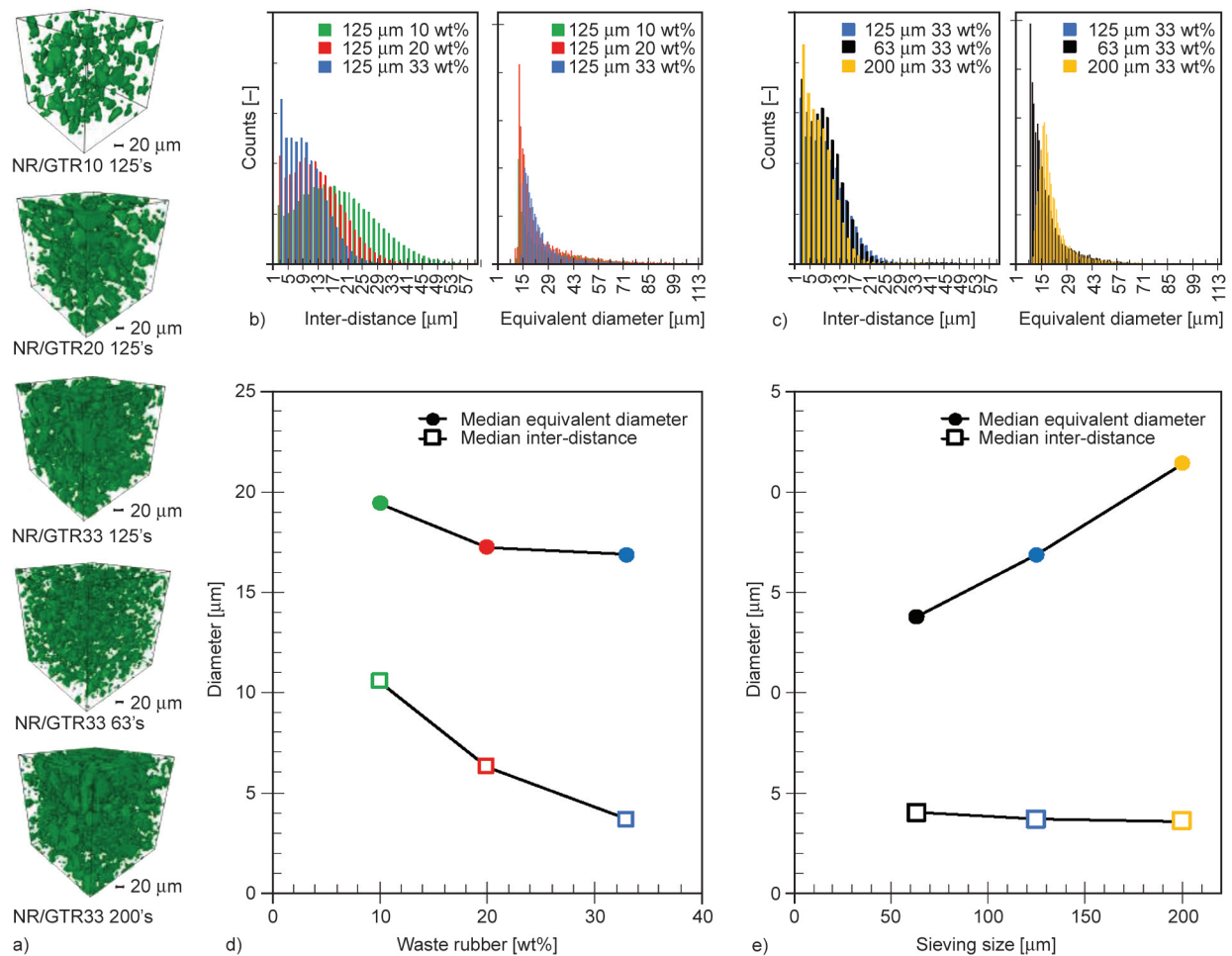

Figure 1. a) 3D representative tomography images of the NR/GTR composites detailed in Table 1, b) distribution of interparticles distances and equivalent diameter distribution for the composites with different contents of waste rubber particles, c) distribution of inter particles distances and equivalent diameter distribution for composites containing waste rubber particles of different average sizes, d) median equivalent diameter and median inter-distance of the composites with different contents of waste rubber for particles sieved at 120 mesh size (size < 125 μm), and e) median equivalent diameter and median inter-distance of the composites containing waste rubber particles of different average sizes, for particles content of 33 wt%.
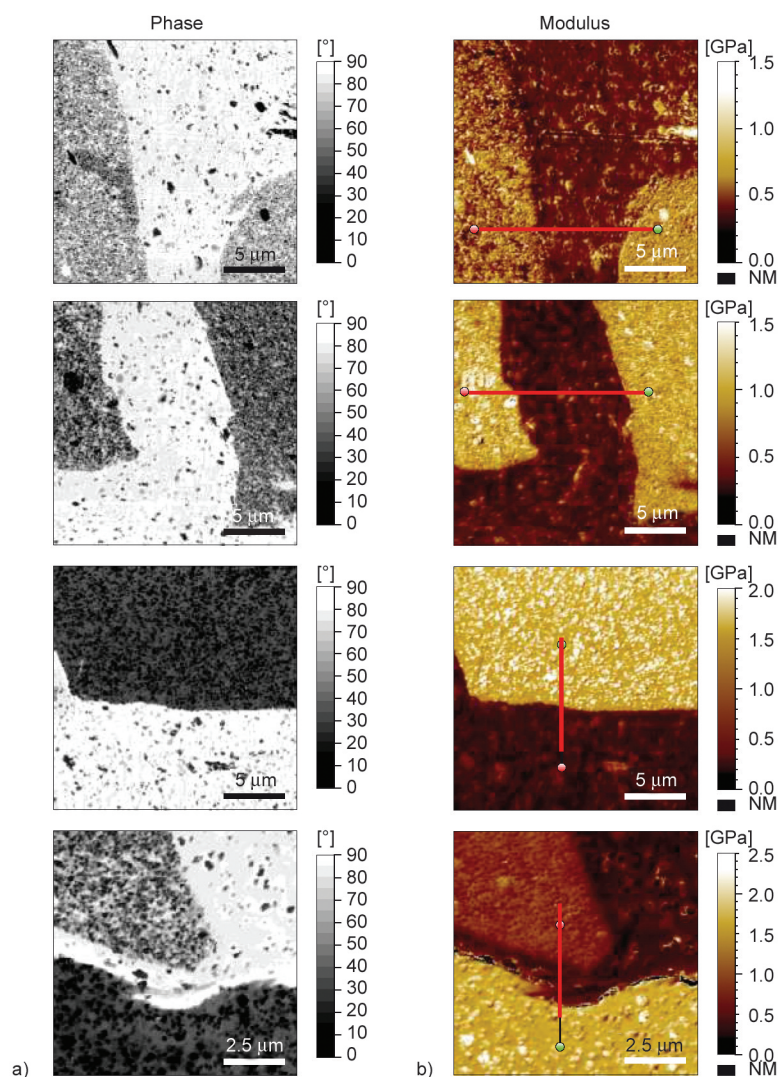
Figure 2. a) Phase contrast images and b) nanomechanical properties of the samples acquired under ambient conditions (room temperature and relative humidity of about 50%). The first and second resonant frequencies for topography measurements were about 280 kHz and ~1.6 MHz for the measurement of the modulus, respectively.

as can be seen on modulus cartographies (Figure 2b top) where the rubber from the matrix and inside the GTR particles appear with high phase (in white) and associated with low modulus (brown). Micron-sized particles present in the NR matrix are most probably related to talc particles arising from the grinding process and dispersed in the matrix during the mixing step. Nano-sized carbon black aggregates are seen in the GTR particles, associated with dark phase contrast and high modulus. These aggregates seem to be of different sizes and densities depending on the observed GTR particle, as they appear with different contrast in phase images and modulus cartographies. However, there is no clear evidence of carbon black aggregates outside the GTR particles. Micron-sized particles are also seen in the GTR particles, likely

arising from residues of the vulcanization process in the pneumatic tire, such as ZnO/Zn stearate.

Strikingly, a difference in phase contrast in the rubber phase of the waste particles is observed. It may result from different types of vulcanized rubber in the waste particles, namely 'soft' and 'hard' seem to appear and can clearly be identified by plotting the modulus distribution (Figure 3a) and the modulus profiles (Figure 3b), where the 'soft' particles appear in blue and 'hard' particles in red, and the natural rubber matrix is plotted in green. This may be related to the binary nature of the GTR particles, which likely contain a major proportion of NR and a minor proportion of SBR. Both have different degrees of unsaturation, which may result in a possible uneven distribution of crosslinks [46]. Moreover, the NR/SBR

composition had been confirmed previously by thermogravimetric analysis (TGA) [47]. The reported values of elastic modulus, or so-called effective elastic modulus, allowed to measure heterogeneities in other types of nano/micro-composites such as shale material [48] or in micrometric materials such as phase change materials (PCM) [49]. In addition, one may note that the high values of room temperature elastic modulus are due to the high resonant frequency ~MHz that affects the mechanical response of the elastomers, which tend to behave as if they were probed at a lower temperature (glassy state). The three populations, NR matrix, 'soft' GTR, and 'hard' GTR, are reported (Figure 3c) where the modulus of rubber phase in the GTR and the carbon black aggregates could have been separated from the clear variations of the modulus profiles in the GTR that show a maximum when passing through CB and minimum value when passing through rubber matrix. Finally, the increasing elastic modulus in NR, NR/SBR matrix of the GTR and CB in the GTR in the rubber phase, respectively, is supposedly beneficial to distribute the stress while the NR/GTR composite is subjected to a large strain, and hence would participate in the deformation mechanisms such as

strain-induced crystallization or elastocaloric effect as will be investigated hereafter.

3.2. Slow strain rate tensile properties and strain-induced crystallization

Vulcanized NR and NR/GTR composites containing GTR with various sizes and weight fractions were processed. Slow strain rate tensile tests at room temperature using *in-situ* WAXS (Figure 4) were performed. Tensile tests show hyper-elastic behavior. A large strain reinforcement is seen at a large strain before the failure of the materials (Figure 4b, 4d). The gaussian approximation describes the entropy changes upon loading that results in an elastic force, written in a simplistic form, as Equation (3) [50]:

$$\sigma_g = \frac{E_c}{3}\left(\lambda - \frac{1}{\lambda_c^2}\right) \qquad (3)$$

with $E_c = 3\nu RT$, E_c is the elastic modulus of the resulting composite, ν is the network chains density [mol·cm^{-3}], $R = 8.314$ J·K^{-1}·mol^{-1}, is the gas constant, T the temperature [K], and $\lambda_c = 1 + \varepsilon$ the strain. The experimental stress-strain curves follow the Gaussian approximation up to a critical strain of around 200%. Above such critical strain, the experimental
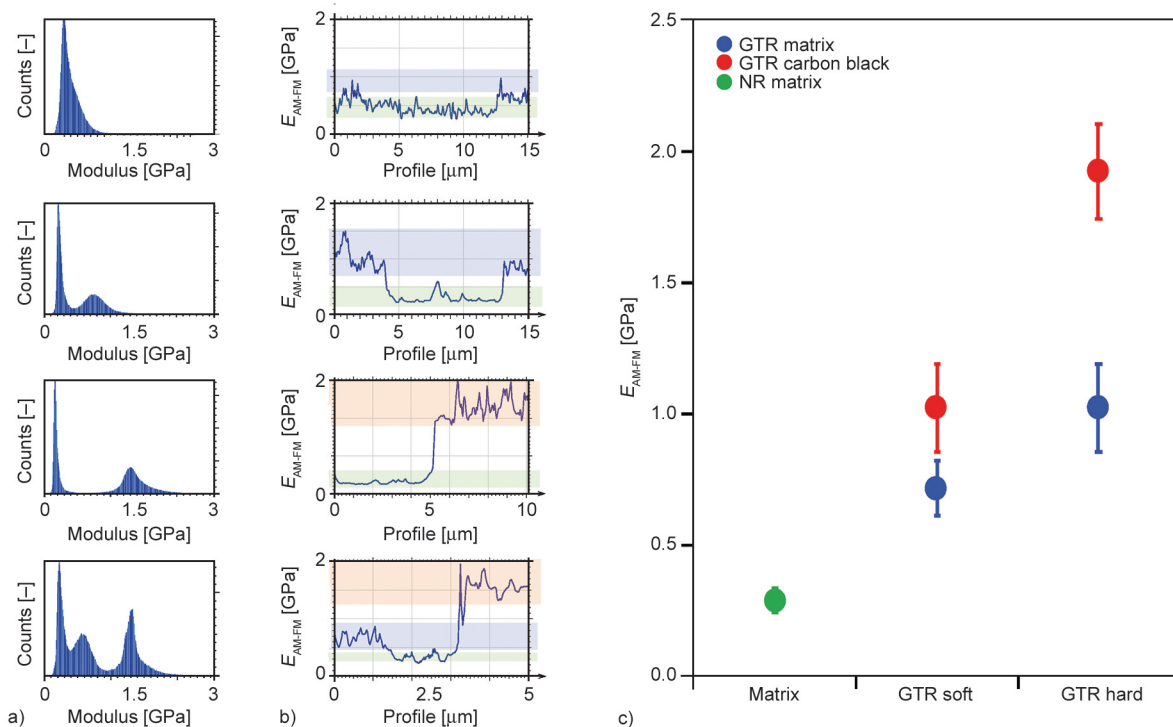

Figure 3. a) Distribution of the elastic modulus extracted from the 2D modulus cartographies shown in Figure 2b, b) profiles of the elastic modulus for selected sections extracted from the same 2D modulus cartographies (the red lines in Figure 2b from red point to green point), c) the reported values of elastic modulus (E_{AM-FM}), or so-called effective elastic modulus estimated from the different regions of the specimen tested, where 'soft' and 'hard' represent different regions in the waste rubber particles.

curve deviates from the Gaussian approximation, suggesting a non-Gaussian reinforcement, likely due to chains limit extensibility and/or SIC. SIC had indeed shown to occur in our composites, as illustrated by the occurrence of typical SIC features as observed during in situ WAXS (Figure 4a). The 2D-WAXS patterns show the progressive appearance of crystalline plane reflections (002), (200), (120) and (210) of the monoclinic crystal structure [51] with the chains axis oriented in the tensile direction. This indicates a transformation from an isotropic amorphous phase in the undeformed state to an anisotropic semi-crystalline phase in the deformed state. The WAXS crystallinity index (Equation 2), suggests the appearance of a crystalline phase at around 300% of deformation for the vulcanized NR (Figure 4c). The crystalline phase appears at a lower strain in the NR/GTR composites which indicates a nucleation

ability of the GTR particles on SIC. The such nucleating effect is likely due to (i) the increase of GTR fraction as a reinforcing phase and (ii) the decrease of inter-distance GR particles, both contributing to the increase of strain localization in the natural rubber at the origin of SIC and then mechanical reinforcement. Contrarily, the modification of the GTR particle size from sieving while maintaining the GTR content appears to play a small role in both crystallization and mechanical reinforcement (Figure 4d, 4e). This is consistent with the invariance of the inter-distance between GTR particles while varying particle sizes (Figure 2), as the latter controls the level of strain localization in the regions that connect the GTR particles. One may note, however, that the limitation of μCT at the micron scale impedes fully detecting the inter-distances at the nanometric scale, where highly stretched regions may connect the
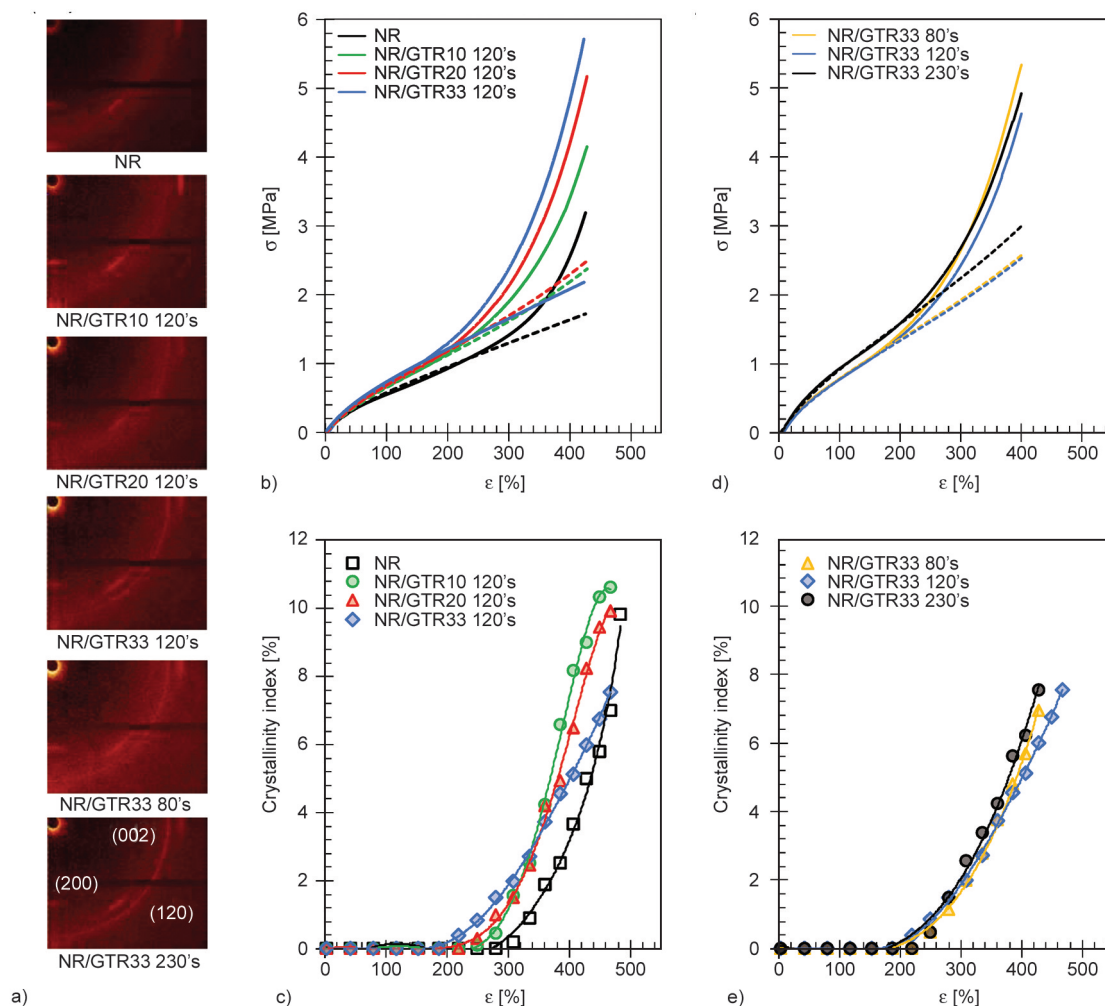

Figure 4. a) 2D WAXS patterns of the NR and NR-GTR composites at the deformation of 500% and after subtraction of the direct beam, b), c) room temperature stress-strain curves of NR and NR/GTR composites. The dotted lines are fits from Gaussian behavior (Equation (3)). d), e) Crystallinity index calculated from Equation (2) for the same series of materials.

particles, as predicted in the case of carbon black-filled rubber [52, 53]. Nonetheless, they should control the occurrence of only a limited fraction of the crystalline phase and hence marginally participate in mechanical reinforcement related to SIC.

3.3. High strain rate tensile properties and elastocaloric effect

In the previous section, we have suggested that the concomitant increase in GTR fraction and decrease in their inter-distance localizes the strain into the NR matrix and hence participate in the nucleation mechanisms of SIC and subsequent mechanical reinforcement. In this section, the effect of these particles on the elastocaloric effects (Figure 5 and Figure 6) and their possible spatial distribution (Figure 7) are studied. First, incremental cyclic tests were performed at a high strain rate ($5.6 \cdot 10^1$ min^{-1}) so that near-adiabatic conditions were reached, and temperature changes were measured on the surface of the specimens by an infrared camera. Cyclic tests are chosen as it gives access at the same time to two SIC signatures through (i) mechanical energy dissipation and through (ii) the heating/cooling arising from the latent heat of crystallization/melting during loading/unloading. For both approaches, the contributions to both mechanical dissipation and heat exchanges of deformation mechanisms other than strain-induced crystallization/melting must be evaluated. It has been shown that most of the mechanical hysteresis arising from cyclic tensile tests in natural rubber originates from SIC [54, 55]. More specifically, strain-induced crystallization starts at a strain, λ_c, during loading, and complete melting occurs at a strain, λ_m. λ_m is always found lower than λ_c due to what we call the superstraining effect [56]. This superstraining effect is analogous to the well-known supercooling effect occurring during thermal crystallization, where the melting temperature, T_m, is higher that the crystallization temperature, T_c. Damage induced by cavitation and strain-induced crystallization in filled natural rubber are two competitive mechanisms [57, 19]. However, damage in NR/GTR blends is expected to be less present as compared to conventional industrial-filled rubber [58, 59] where the volume fraction of cavities can be measured up to 50%, concomitantly occurring with a dissipative thermal signature [60, 61]. Damage mechanism via cavitation is expected to be negligible in our materials due to the relatively low amount of carbon black, with a maximum of 7.8 vol% in the

case of NR/GTR33. The calculation of the value of 7.8 vol% can be found in a previous publication (Table 1, [26]).

The temperature rise on a rubber specimen surface generated during rapid loading has been shown in the case of vulcanized NR [34]. Like the vulcanized NR, in the vulcanized NR/GTR composites, it can be induced by thermoelastic effects, crystallization or viscosity. The contribution of thermoelastic effects to heating temperature, θ_{th-e}, can be estimated within the frame of the Gaussian approximation (Equation (4)):

$$\theta_{th-e} = \frac{T}{\rho C_p} \int_1^\lambda \left(\frac{\partial \sigma_g}{\partial T}\right)_\lambda d\lambda \tag{4}$$

where σ_g is given by Equation (3). From the work of Guth [62]. ρ [g·cm^{-3}] and C_p are the density and specific heat capacity [J·g^{-1}·°C^{-1}] of the materials respectively. Equation (5) results in an expression of the temperature change that accounts for the local strain of the natural rubber matrix, λ_{local}, (expectedly higher that the macroscopic strain, λ, in presence of undeformable carbon black particles) (Equation (5)):

$$\theta_{th-e} = \frac{\nu RT}{2\rho C_p} \left(\lambda_{local}^2 + \frac{2}{\lambda_{local}} - 3\right) \tag{5}$$

where the parameter νRT had been defined above in the explanation of Equation (3). The estimate of the local strain, λ_{local}, had been estimated previously for each type of blend and can be found in previous work [26]. In vulcanized NR, the dissipated energy had been found to be essentially related to SIC, as no hysteresis had been detected before SIC initiation [54]. In this study, we decided not to express this term for the sake of simplicity, and its contribution may be implicitly involved in the thermoelastic term. This suggests that the viscoelastic effect may intervene in the calculation of the elastic modulus (as a result, for instance, of additional trapped entanglements due to a high strain rate). Like for the single tensile tests, cyclic tests were fitted with Gaussian approximation (Figure 5a) and the temperature by approximation of thermoelastic effect (Figure 5b). The experimental temperature rise is found to deviate from the thermoelastic contribution at the critical strain of around 300% for vulcanized NR. It is found below 300% for the vulcanized NR/GTR blends (Figure 5b). It occurs simultaneously as compared to the deviation of the experimental mechanical response from the Gaussian behavior (Figure 5a). The subtraction of
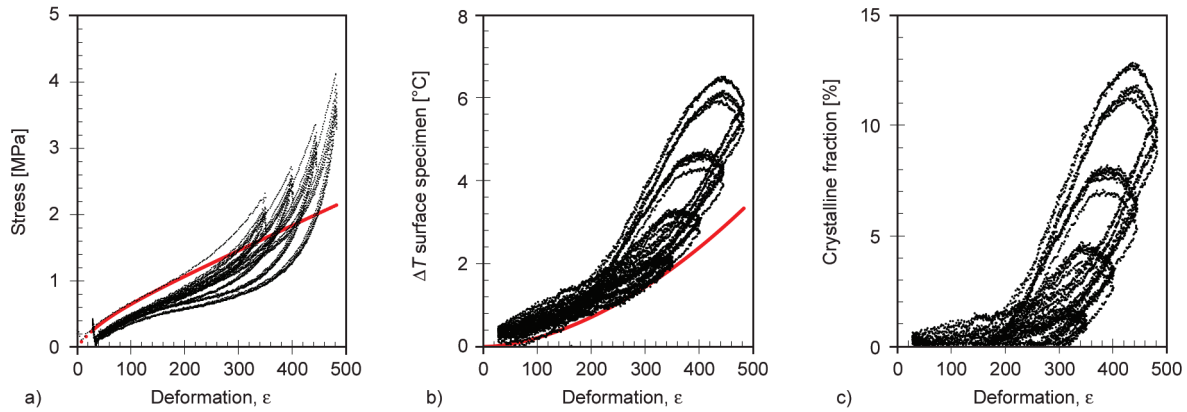
Figure 5. a) Stress strain curve for incremental cycles. The cyclic test consists in a series of 5 cycles performed at incremental strain (3 in total) and for each cycle the mechanical hysteresis is characterized by the area between loading and unloading curves. The red continuous line represents the fit for gaussian behaviour. b) Temperature changes observed on the specimen surface during the cyclic test. The temperature at the beginning of each cycle has been adjusted to room temperature for sake of simplicity. The red continuous line represents the temperature rise induced by thermoelastic effects as estimated from Equation (5). c) Crystalline fraction measured from the changes in surface temperature and from Equation (6).

the thermoelastic effects on the total heating allows us to quantify the heating associated with SIC $\theta_\chi = \theta - \theta_{th\text{-}e}$. The volume fraction of strain induced crystals is then given by Equation (6) [63, 26]:

$$\chi \approx \rho C_p \frac{\theta_\chi}{(1 - \varphi_f)\Delta H_m} \tag{6}$$

where ρ and C_p are the density and specific heat capacity of the materials, respectively. $\Delta H_m = 61$ MJ·m^{-3} the melting enthalpy of vulcanized NR [64] and φ_f is the volume fraction of carbon black fillers. Equation (6) accounts for the crystalline fraction that is corrected to the presence of carbon black particles, hence only considering the rubber fraction, $1 - \varphi_f$ (Table 1).

The mechanical hysteresis and crystalline fraction are presented using the data shown for the NR/GTR20 120's blend, and the same data was extracted for the pristine NR for the sake of comparison (Figure 6). NR/GTR20 120's blend had been chosen so that the involved waste rubber particles are not too big so that it avoids premature failure during cyclic loading and, at the same time, not to fine, as the latter is more difficult to obtain through sieving, and do not necessarily provide better crystallization properties (Figure 4e). The mechanical hysteresis is simply calculated as the area under the curve for each strain step of the incremental loading/ unloading test (Figure 6a). The crystallinity index is the maximum value measured at the end of the loading
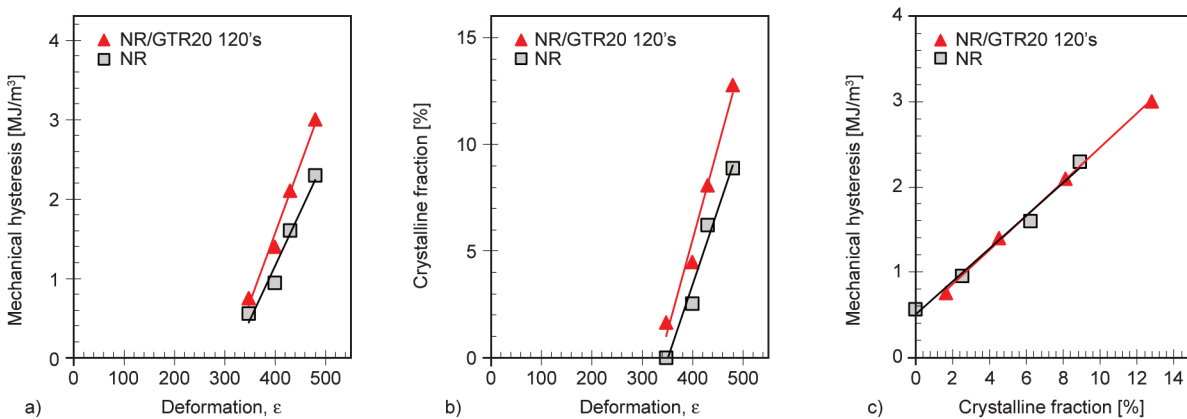

Figure 6. a) Mechanical hysteresis measured from area under the curve versus applied deformation for the NR and NR/GTR20 120's blend, b) crystalline fraction measured from the changes in surface temperature and from Equation (6) plotted as a function of the deformation, c) mechanical hysteresis as a function of the crystalline fraction measured at the end of the first loading at each strain of the incremental tensile test.

for each strain step. For the sake of clarity, in Figure 6, only the mechanical hysteresis and crystallinity index measured at the 5th (ultimate) cycle of each incremental step had been reported and plotted as a function of the maximum applied strain. After 5 cycles, both mechanical hysteresis and crystallinity index are found to be stable with cyclic accumulation. Compared to the reference NR, the NR/GTR20 120's composite shows higher mechanical dissipation for a given strain, consistent with the observed nucleation ability of the waste rubber particles on SIC, as previously demonstrated during slow tensile tests by situ WAXS. The crystalline fraction measured from latent heat (Figure 6b) results in a similar trend as compared to the WAXS crystallinity index: (i) the absolute values are not far away between the two tests, (ii) the strain at crystallization onset is slightly lower in the fast tensile test, likely explained by a delay in SIC, (iii) the crystalline fraction is higher in NR/GTR20 as compared to NR, confirming the nucleation effect of the GTR particles during the high strain rate tests, and also consistent with the observed shift in the mechanical hysteresis. Finally, the plot of the mechanical hysteresis versus the crystalline fraction indicates linear dependence (Figure 6c), independently of the tested material, suggesting these two quantities have a close correlation. The initial value of the mechanical hysteresis at zero crystallinity suggests the pre-existence of a mechanical hysteresis before the occurrence of SIC, which might be induced by dissipative viscoelastic effects that may arise from high strain rate conditions. In contrast, such effects had not been observed previously in the literature at lower strain rate conditions [54]. To access more local information on elastocaloric properties related to the distribution of waste rubber particles, an infra-red camera was placed closer to the rubber specimen to get a higher resolution (cf. Section 2.6.). The temperature at the specimen surface was tracked during the following test: fast loading (α, β), relaxation in the deformed state (β, γ), fast unloading (δ, ε) and maintenance in the relaxed state (ε, ζ), as seen on Figures 7a, 7b. A micron scale observation of the elastocaloric effect in NR reveals a slight anisotropy with filament-like features oriented along the stretching axis. This is consistent with thermal features associated with entropic elasticity and latent heat arising from thermoelastic effect and SIC, respectively and that occur due to the high orientation of the rubber chains along the stretching axis.

Contrarily, the NR/GTR blends show distinct elastocaloric features. Temperature heterogeneities are induced by the presence of waste particles, which are clearly visualized by increasing the image contrast (Figures 7c, 7d). It seems that the surrounding areas of the particles show slightly higher heating during loading that may arise from stress concentration in their vicinity, near the interface with the NR matrix. Conversely, during cooling, the same type of localized areas, of the size of the waste particles, are found colder as compared to the matrix. This likely arises from localized strain, inducing localized thermoelastic effect and SIC during loading and hence subsequent higher cooling due to release of these to effects.

The relative temperature fluctuation [%] during the tests had also been measured as σ/|T| with T the average temperature specimen and σ the absolute temperature fluctuation around T. This relative temperature fluctuation is difficult to interpret during the tests, as the area under analysis is moving. Nonetheless, just before loading and right after unloading, states (α) and (ε), respectively, can be compared as the same specimen area is analyzed. State (α) serves as a reference indicating a pre-existing relative temperature fluctuation prior to the tensile test, that is equal to 0.8% (corresponding to an absolute temperature fluctuation of ±0.27 °C) and 0.6% (corresponding to an absolute temperature fluctuation of ±0.20 °C) in case of NR and NR/GTR respectively likely arising from differences in the emissivity due to irregularities on the specimen surface, inclination in the specimen in the area studied or due to the presence of wastes containing CB fillers. One may note that the surface emissivity of carbon black filled rubber is close to a black body one and is fixed at 0.94 [65] or above [65, 66], and shown to not depend on the carbon black content [66] nor on the applied deformation [67]. Right after the end of the unloading, relative temperature fluctuation is found to equal 0.8% (corresponding to an absolute temperature fluctuation of ±0.27 °C) in the case of NR, which is the exact same value as before loading. Nonetheless, it is found to equal 1.1% (corresponding to an absolute temperature fluctuation of ±0.37 °C) in the case of NR/GTR blend, an increment of ±0.17 °C as compared to fluctuation before the tensile test. This is likely due to remaining temperature heterogeneities in the surrounding region of waste particles, likely due to the discharge of the local stress associated
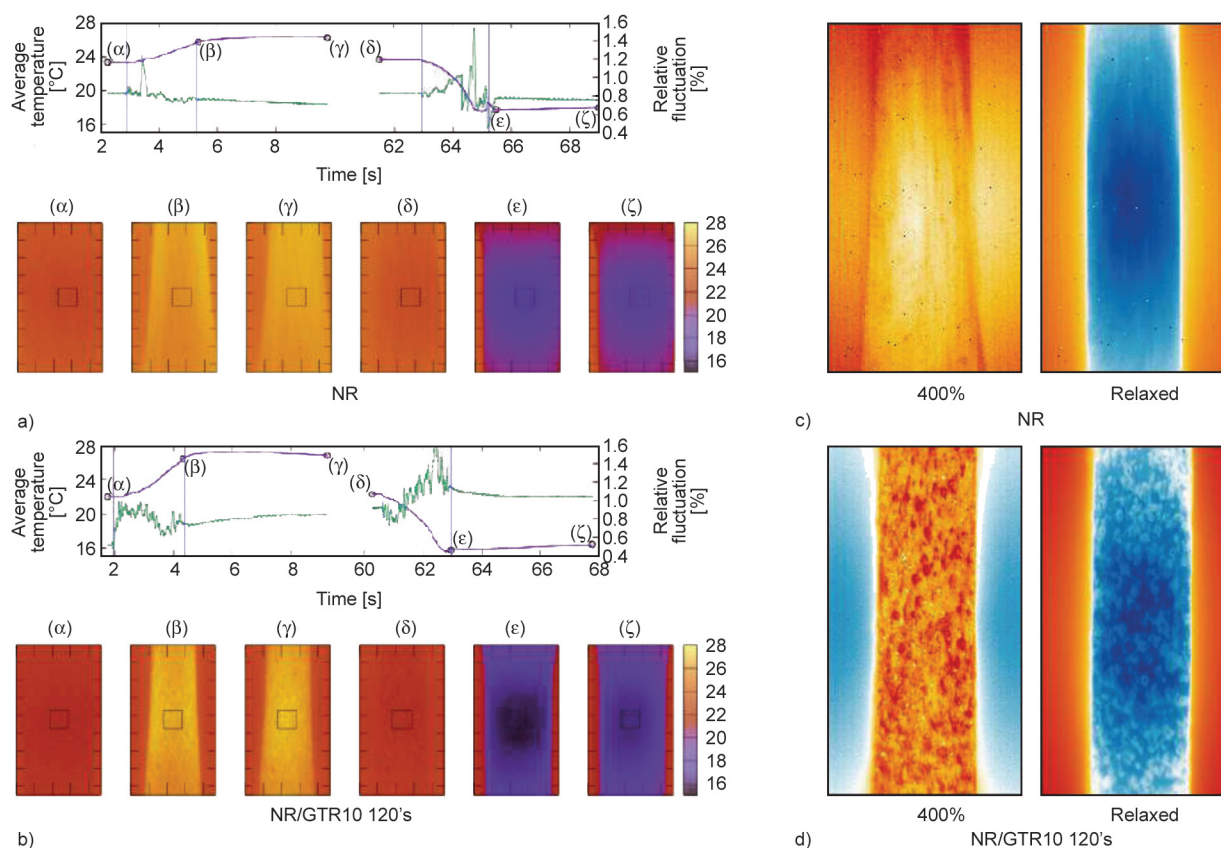
Figure 7. Average temperature and relative fluctuation of temperature at the specimen surface during fast loading (α), (β), relaxation in the deformed state (β), (γ), fast unloading (δ), (e), and relaxation in the undeformed state (ε), (ζ) for NR (a) and NR/GTR10 (b). Images were recorded during the loading phase at around 400% of deformation (top figure) and at the end of unloading (bottom figure) with high contrast for NR (c) and NR/GTR10 (d), respectively.

with the release of entropic elasticity and melting of SIC crystals.

4. Conclusions

Ground tire rubber particles (GTR) of different sizes and contents were blended with natural rubber (NR) and vulcanized to prepare crystallizable composites with elastocaloric properties. A µCT study suggests both the decreasing inter-distance between particles in conjunction with their increasing content is expected to favor strain localization upon tensile deformation. A more local study at GTR/matrix interface by AFM suggests a certain inter-melling between the NR matrix and the GTR particles. Two populations of particles were observed in the composites, related to the binary nature of the GTR particles, likely containing NR and SBR, with uneven distribution of crosslinks and carbon black contents. The differential mechanical properties between the matrix and particles are supposedly beneficial to distribute the stress while the NR/GTR composite is subjected to a large strain and hence would participate

in the deformation mechanisms such as strain-induced crystallization or elastocaloric effect. Tensile deformation of the NR/GTR blends shows a nucleating ability of the GTR particles on strain-induced crystallization and elastocaloric properties independently of the particle size. Finally, a local study of the temperature field induced by mechanical deformation show surrounding areas of the particles whose heating during loading is found to be slightly higher that may arise from stress concentration in their vicinity, near the interface with the NR matrix. Conversely, during cooling, the same type of localized areas, of the size of the waste particles, are found to be colder as compared to the matrix. We believe that this study can open a perspective on the heat transfer in waste-based rubber composites. For instance, questions on thermal diffusion at waste particles and the NR matrix or on the precise nature of the local heat transfer would be of great interest. Understanding and controlling heat/cool localization in such materials should be crucial to designing waste rubber-based specimens for efficient cooling technology.

Acknowledgements

References

[1] Grocholski B.: Cooling in a warming world. Science, **37**, 776–777 (2020).
https://doi.org/10.1126/science.abf1931

[2] Goetzler W., Zogg R., Young J., Johnson C.: Energy savings potential and RD&D opportunities for non-vapor-compression HVAC technologies. EERE Publication and Product Library, Washington (2014).

[3] Greco A., Aprea C., Maiorino A., Masselli A.: A review of the state of the art of solid-state caloric cooling processes at room-temperature before 2019. International Journal of Refrigeration, **106**, 66–88 (2019).
https://doi.org/10.1016/j.ijrefrig.2019.06.034

[4] Pecharsky V. K., Gschneidner K. A.: Giant magnetocaloric effect in $Gd_5(Si_2Ge_2)$. Physical Review Letters, **78**, 4494–4497 (1997).
https://doi.org/10.1103/PhysRevLett.78.4494

[5] Neese B., Chu B., Lu S-G., Wang Y., Furman E., Zhang Q. M.: Large electrocaloric effect in ferroelectric polymers near room temperature. Science, **321**, 821–823 (2008).
https://doi.org/10.1126/science.1159655

[6] Bonnot E., Romero R., Mañosa L., Vives E., Planes A.: Elastocaloric effect associated with the martensitic transition in shape-memory alloys. Physical Review Letters, **100**, 125901 (2008).
https://doi.org/10.1103/PhysRevLett.100.125901

[7] Mañosa L., González-Alonso D., Planes A., Bonnot E., Barrio M., Tamarit J. L., Aksoy S., Acet M.: Giant solid-state barocaloric effect in the Ni–Mn–In magnetic shape-memory alloy. Nature Materials, **9**, 478–481 (2010).
https://doi.org/10.1038/nmat2731

[8] Moya X., Mathur N. D.: Caloric materials for cooling and heating. Science, **370**, 797–803 (2020).
https://doi.org/10.1126/science.abb0973

[9] Qian S., Geng Y., Wang Y., Ling J., Hwang Y., Radermacher R., Takeuchi I., Cui J.: A review of elastocaloric cooling: Materials, cycles and system integrations. International Journal of Refrigeration, **64**, 1–19 (2016).
https://doi.org/10.16/j.ijrefrig.2015.12.001

[10] Tušek J., Engelbrecht K., Eriksen D., Dall'Olio S., Tušek J., Pryds N.: A regenerative elastocaloric heat pump. Nature Energy, **1**, 16134 (2016).
https://doi.org/10.38/nenergy.2016.134

[11] Coativy G., Haissoune H., Seveyrat L., Sebald G., Chazeau L., Chenal J-M., Lebrun L.: Elastocaloric properties of thermoplastic polyurethane. Applied Physics Letters, **117**, 193903 (2020).
https://doi.org/10.63/5.0023520

[12] Xie Z., Sebald G., Guyomar D.: Comparison of elastocaloric effect of natural rubber with other caloric effects on different-scale cooling application cases. Applied Thermal Engineering, **111**, 914–926 (2017).
https://doi.org/10.1016/j.applthermaleng.2016.09.164

[13] Candau N., Stoclet G., Tahon J-F., Demongeot A., Yilgor E., Yilgor I., Menceloglu Y. Z., Oguz O.: Mechanical reinforcement and memory effect of strain-induced soft segment crystals in thermoplastic polyurethane-urea elastomers. Polymer, **223**, 123708 (2021).
https://doi.org/10.1016/j.polymer.2021.123708

[14] Huneau B.: Strain-induced crystallization of natural rubber: A review of X-ray diffraction investigations. Rubber Chemistry Technology, **84**, 425–452 (2011).
https://doi.org/10.5254/1.3601131

[15] Trabelsi S., Albouy P-A., Rault J.: Stress-induced crystallization properties of natural and synthetic cis-polyisoprene. Rubber Chemistry Technology, **77**, 303–316 (2004).
https://doi.org/10.5254/1.3547825

[16] Candau N., Chazeau L., Chenal J-M., Gauthier C., Munch E.: A comparison of the abilities of natural rubber (NR) and synthetic polyisoprene cis-1,4 rubber (IR) to crystallize under strain at high strain rates. Physical Chemistry Chemical Physics, **18**, 3472–3481 (2016).
https://doi.org/10.1039/C5CP06383C

[17] Trabelsi S., Albouy P-A., Rault J.: Effective local deformation in stretched filled rubber. Macromolecules, **36**, 9093–9099 (2003).
https://doi.org/10.1021/ma0303566

[18] Candau N., Chazeau L., Chenal J-M., Gauthier C., Munch E.: Compared abilities of filled and unfilled natural rubbers to crystallize in a large strain rate domain. Composites Science and Technology, **108**, 9–15 (2015).
https://doi.org/10.1016/j.compscitech.2014.12.014

[19] Chenal J-M., Gauthier C., Chazeau L., Guy L., Bomal Y.: Parameters governing strain induced crystallization in filled natural rubber. Polymer, **48**, 6893–6901 (2007).
https://doi.org/10.1016/j.polymer.2007.09.023

[20] Xie Z-T., Luo M-C., Huang C., Wei L-Y., Liu Y-H., Fu X., Huang G., Wu J.: Effects of graphene oxide on the strain-induced crystallization and mechanical properties of natural rubber crosslinked by different vulcanization systems. Polymer, **151**, 279–286 (2018).
https://doi.org/10.1016/j.polymer.2018.07.067

[21] Nie Y., Huang G., Qu L., Wang X., Weng G., Wu J.: New insights into thermodynamic description of strain-induced crystallization of peroxide cross-linked natural rubber filled with clay by tube model. Polymer, **52**, 3234–3242 (2011).
https://doi.org/10.1016/j.polymer.2011.05.004

[22] Salleh S. Z., Ahmad M. Z., Ismail H.: Properties of natural rubber/recycled chloroprene rubber blend: Effects of blend ratio and matrix. Procedia Chemistry, **19**, 346–350 (2016).
https://doi.org/10.1016/j.proche.2016.03.022

[23] Mathew G., Singh R. P., Nair N. R., Thomas S.: Recycling of natural rubber latex waste and its interaction in epoxidised natural rubber. Polymer, **42**, 2137–2165 (2001).
https://doi.org/10.1016/S0032-3861(00)00492-4

[24] Zhang X., Lu C., Liang M.: Properties of natural rubber vulcanizates containing mechanochemically devulcanized ground tire rubber. Journal of Polymer Research, **16**, 411–419 (2009).
https://doi.org/10.1007/s10965-008-9243-x

[25] Candau N., Oguz O., Federico C. E., Stoclet G., Tahon J-F., Maspoch M. L.: Strain induced crystallization in vulcanized natural rubber containing ground tire rubber particles with reinforcement and nucleation abilities. Polymer Testing, **101**, 107313 (2021).
https://doi.org/10.1016/j.polymertesting.2021.107313

[26] Candau N., Vives E., Fernández A. I., Maspoch M. L.: Elastocaloric effect in vulcanized natural rubber and natural/wastes rubber blends. Polymer, **236**, 124309 (2021).
https://doi.org/10.1016/j.polymer.2021.124309

[27] Dart S. L., Anthony R. L., Guth E.: Rise of temperature on fast stretching of synthetics and natural rubbers. Industrial and Engineering Chemistry, **34**, 1340–1342 (1942).
https://doi.org/10.1021/ie50395a020

[28] Flory P. J.: Thermodynamics of crystallization in high polymers. I. Crystallization induced by stretching. Journal of Chemical Physics, **15**, 397–408 (1947).
https://doi.org/10.1063/1.1746537

[29] Mistry S. J., Govindjee S.: A micro-mechanically based continuum model for strain-induced crystallization in natural rubber. International Journal of Solids and Structures, **51**, 530–539 (2014).
https://doi.org/10.1016/j.ijsolstr.2013.10.027

[30] Plagge J., Hentschke R.: Microphase separation in strain-crystallizing rubber. Macromolecules, **54**, 5629–5635 (2021).
https://doi.org/10.1021/acs.macromol.1c00757

[31] Laghmach R., Candau N., Chazeau L., Munch E., Biben T.: Phase field modelling of strain induced crystal growth in an elastic matrix. The Journal of Chemical Physics, **142**, 244905 (2015).
https://doi.org/10.1063/1.4923226

[32] Xie Z., Sebald G., Guyomar D.: Elastocaloric effect dependence on pre-elongation in natural rubber. Applied Physics Letters, **107**, 081905 (2015).
https://doi.org/10.1063/1.4929395

[33] Guyomar D., Li Y., Sebald G., Cottinet P-J., Ducharne B., Capsal J-F.: Elastocaloric modeling of natural rubber. Applied Thermal Engineering, **57**, 33–38 (2013).
https://doi.org/10.1016/j.applthermaleng.2013.03.032

[34] Xie Z., Sebald G., Guyomar D.: Temperature dependence of the elastocaloric effect in natural rubber. Physics Letters A, **381**, 2112–2116 (2017).
https://doi.org/10.1016/j.physleta.2017.02.014

[35] Candau N., Chazeau L., Chenal J-M., Gauthier C., Ferreira J., Munch E., Rochas C.: Characteristic time of strain induced crystallization of crosslinked natural rubber. Polymer, **53**, 2540–2543 (2012).
https://doi.org/10.1016/j.polymer.2012.04.027

[36] European Commission: A European strategy for plastics in a circular economy. Brussels (2018).

[37] Sienkiewicz M., Janik H., Borzędowska-Labuda K., Kucińska-Lipka J.: Environmentally friendly polymer-rubber composites obtained from waste tyres: A review. Journal of Cleaner Production, **147**, 560–571 (2017).
https://doi.org/10.1016/j.jclepro.2017.01.121

[38] Bom N. M., Usuda É. O., da Silva Gigliotti M., de Aguiar D. J. M., Imamura W., Paixão L. S., Carvalho A. M. G.: Waste tire rubber-based refrigerants for solid-state cooling devices. Chinese Journal of Polymer Science, **38**, 769–775 (2020).
https://doi.org/10.1007/s10118-020-2385-y

[39] Ranc N., Wagner D.: Some aspects of Portevin–Le Chatelier plastic instabilities investigated by infrared pyrometry. Materials Science and Engineering: A, **394**, 87–95 (2005).
https://doi.org/10.1016/j.msea.2004.11.042

[40] Bodelot L., Charkaluk E., Sabatier L., Dufrénoy P.: Experimental study of heterogeneities in strain and temperature fields at the microstructural level of polycrystalline metals through fully-coupled full-field measurements by digital image correlation and infrared thermography. Mechanics of Materials, **43**, 654–670 (2011).
https://doi.org/10.1016/j.mechmat.2011.08.006

[41] Shen Y., Sun W., Wei Z. Y., Shen Q., Zhang Y. F., Liu J.: Orientation dependent elastocaloric effect in directionally solidified Ni-Mn-Sn alloys. Scripta Materialia, **163**, 14–18 (2019).
https://doi.org/10.1016/j.scriptamat.2018.12.026

[42] Jongchansitto K., Jongchansitto P., Preechawuttipong I., Balandraud X., Grédiac M., Le Cam J-B., Blanchet F.: Using IR thermography to analyze the mechanical response of a granular material. International Journal of Mechanical Engineering and Robotics Research, **10**, 189–195 (2021).
https://doi.org/10.18178/ijmerr.10.4.189-195

[43] Candau N., Oguz O., Albiter N. L., Förster G., Maspoch M. L.: Poly(Lactic acid)/ground tire rubber blends using peroxide vulcanization. Polymers, **13**, 1496 (2021).
https://doi.org/10.3390/polym13091496

[44] Kruželák J., Sýkora R., Hudec I.: Peroxide vulcanization of natural rubber. Part I: Effect of temperature and peroxide concentration. Journal of Polymer Engineering, **34**, 617–624 (2014).
https://doi.org/10.1515/polyeng-2014-0034

[45] Federico C. E., Rauchs G., Kotecky O., Westermann S., Addiego F.: Cavitation in thermoplastic-reinforced rubber composites upon cyclic testing: Multiscale characterization and modelling. Polymer, **211**, 123084 (2020).
https://doi.org/10.1016/j.polymer.2020.123084

[46] Cosas Fernandes J. P., Federico C. E., Lentzen E., Valle N., Basterra-Beroiz B., Weydert M., Quintana R.: Viscoelastic properties and sulfur distribution at the nanoscale in binary elastomeric blends: Toward phase-specific cross-link density estimations. ACS Applied Polymer Materials, **3**, 3287–3297 (2021).
https://doi.org/10.1021/acsapm.1c00032

[47] Candau N., Oguz O., Albiter N. L., Förster G., Maspoch M. L.: Poly(lactic acid)/ground tire rubber blends using peroxide vulcanization. Polymers, **13**, 1496 (2021).
https://doi.org/10.3390/polym13091496

[48] Liu Y., Sokolov I., Dokukin M. E., Xiong Y., Peng P.: Can AFM be used to measure absolute values of Young's modulus of nanocomposite materials down to the nanoscale? Nanoscale, **12**, 12432–12443 (2020).
https://doi.org/10.1039/D0NR02314K

[49] Giro-Paloma J., Oncins G., Barreneche C., Martínez M., Fernández A. I., Cabeza L. F.: Physico-chemical and mechanical properties of microencapsulated phase change material. Applied Energy, **109**, 441–448 (2013).
https://doi.org/10.1016/j.apenergy.2012.11.007

[50] Treloar L. R. G.: The physics of rubber elasticity. Oxford University Press, New York (1975).

[51] Bunn C. W., Bragg W. H.: Molecular structure and rubber-like elasticity I. The crystal structures of β gutta-percha, rubber and polychloroprene. Proceeding of the Royal Society A: Mathematical, Physical and Engineering Science, **180**, 40–66 (1942).
https://doi.org/10.1098/rspa.1942.0024

[52] Tomita Y., Azuma K., Naito M.: Computational evaluation of strain-rate-dependent deformation behavior of rubber and carbon-black-filled rubber under monotonic and cyclic straining. International Journal of Mechanical Sciences, **50**, 856–868 (2008).
https://doi.org/10.1016/j.ijmecsci.2007.09.010

[53] Jiang Y., Shi X., Qiu K.: A micromechanics-based incremental damage model for carbon black filled rubbers. Composites Part B: Engineering, **75**, 11–16 (2015).
https://doi.org/10.1016/j.compositesb.2015.01.027

[54] Rault J., Marchal J., Judeinstein P., Albouy P. A.: Chain orientation in natural rubber, Part II: ^{2}H-NMR study. The European Physical Journal E, **21**, 243–261 (2006).
https://doi.org/10.1140/epje/i2006-10064-6

[55] Le Cam J-B.: Energy storage due to strain-induced crystallization in natural rubber: The physical origin of the mechanical hysteresis. Polymer, **127**, 166–173 (2017).
https://doi.org/10.1016/j.polymer.2017.08.059

[56] Candau N., Laghmach R., Chazeau L., Chenal J-M., Gauthier C., Biben T., Munch E.: Strain-induced crystallization of natural rubber and cross-link densities heterogeneities. Macromolecules, **47**, 5815–5824 (2014).
https://doi.org/10.1021/ma5006843

[57] Le Cam J-B., Toussaint E.: Volume variation in stretched natural rubber: Competition between cavitation and stress-induced crystallization. Macromolecules, **41**, 7579–7583 (2008).
https://doi.org/10.1021/ma801290w

[58] Merckel Y., Diani J., Brieu M., Caillard J.: Effects of the amount of fillers and of the crosslink density on the mechanical behavior of carbon-black filled styrene butadiene rubbers. Journal of Applied Polymer Science, **129**, 2086–2091 (2013).
https://doi.org/10.1002/app.38925

[59] Candau N., Oguz O., Peuvrel-Disdier E., Bouvard J-L., Pradille C., Billon N.: Strain and filler ratio transitions from chains network to filler network damage in EPDM during single and cyclic loadings. Polymer, **197**, 122435 (2020).
https://doi.org/10.1016/j.polymer.2020.122435

[60] Candau N., Oguz O., Peuvrel-Disdier E., Bouvard J-L., Maspoch M. L., Corvec G., Pradille C., Billon N.: Heat source and voiding signatures of Mullins damage in filled EPDM. Polymer Testing, **91**, 106838 (2020).
https://doi.org/10.1016/j.polymertesting.2020.106838

[61] Candau N., Oguz O., Peuvrel-Disdier E., Bouvard J-L., Maspoch M. L., Corvec G., Pradille C., Billon N.: Effect of the strain rate on damage in filled EPDM during single and cyclic loadings. Polymers, **12**, 3021 (2020).
https://doi.org/10.3390/polym12123021

[62] James H. M., Guth E.: Theory of the elastic properties of rubber. The Journal of Chemical Physics, **11**, 455–481 (1943).
https://doi.org/10.1063/1.1723785

[63] Mitchell J. C., Meier D. J.: Rapid stress-induced crystallization in natural rubber. Journal of Polymer Science Part A-2: Polymer Physics, **6**, 1689–1703 (1968).
https://doi.org/10.1002/pol.1968.160061001

[64] Kim H-G., Mandelkern L.: Multiple melting transitions in natural rubber. Journal of Polymer Science Part B: Polymer Physics, **10**, 1125–1133 (1972).
https://doi.org/10.1002/pol.1972.160100614

[65] Loukil M. T., Corvec G., Robin E., Miroir M., Le Cam J-B., Garnier P.: Stored energy accompanying cyclic deformation of filled rubber. European Polymer Journal, **98**, 448–455 (2018).
https://doi.org/10.1016/j.eurpolymj.2017.11.035

[66] Le Saux V., Marco Y., Calloch S., Charrier P.: Contribution of accurate thermal measurements to the characterisation of thermomechanical properties of rubber-like materials. Plastics Rubber and Composites, **41**, 277–284 (2012)
https://doi.org/10.1179/1743289812Y.0000000015

[67] Le Saux V., Marco Y., Calloch S., Charrier P., Taveau D.: Heat build-up of rubber under cyclic loadings: Validation of an efficient demarch to predict the temperature fields. Rubber Chemistry and Technology, **86**, 38–56 (2013).
https://doi.org/10.5254/rct.13.88912